Imaging at an x-ray absorption edge using free electron laser pulses for interface dynamics in high energy density systems

M. A. Beckwith,[1] S. Jiang,[1] A. Schropp,[2] A. Fernandez-Pañella,[1] H. G. Rinderknecht,[1] S. C. Wilks,[1] K. B. Fournier,[1] E. C. Galtier,[3] Z. Xing,[3] E. Granados,[3] E. Gamboa,[3] S. H. Glenzer,[3] P. Heimann,[3] U. Zastrau,[4] B. I. Cho,[5] J. H. Eggert,[1] G. W. Collins,[1] and Y. Ping[1]

[1]*Lawrence Livermore National Laboratory, Livermore, California 94550, USA*
[2]*Deutsches Elektronen-Synchrotron DESY, Hamburg D-22607, Germany*
[3]*Linac Coherent Light Source, SLAC National Accelerator Laboratory, Menlo Park, California 94025, USA*
[4]*European XFEL, Schenefeld D-22869, Germany*
[5]*Department of Physics and Photon Science, Gwangju Institute of Science and Technology, Gwangju 61005, South Korea*

(Received 16 August 2016; accepted 12 April 2017; published online 1 May 2017)

Tuning the energy of an x-ray probe to an absorption line or edge can provide material-specific measurements that are particularly useful for interfaces. Simulated hard x-ray images above the Fe K-edge are presented to examine ion diffusion across an interface between Fe_2O_3 and SiO_2 aerogel foam materials. The simulations demonstrate the feasibility of such a technique for measurements of density scale lengths near the interface with submicron spatial resolution. A proof-of-principle experiment is designed and performed at the Linac coherent light source facility. Preliminary data show the change of the interface after shock compression and heating with simultaneous fluorescence spectra for temperature determination. The results provide the first demonstration of using x-ray imaging at an absorption edge as a diagnostic to detect ultrafast phenomena for interface physics in high-energy-density systems. *Published by AIP Publishing.* [http://dx.doi.org/10.1063/1.4982166]

I. INTRODUCTION

Understanding the physics that occurs at the interface between two materials is important for many areas of high energy density (HED) science defined as pressure larger than 1 Mbar such as, including inertial confinement fusion (ICF) and shock compression science. For example, kinetic processes such as ion diffusion are typically ignored when modeling ICF in commonly applied radiation-hydrodynamics simulations, but recent experimental[1–3] and theoretical[4–7] studies have highlighted the importance of ion diffusion in the ICF process. In shock compression experiments, diffusion at the interfaces between the ablator and the sample, or between the sample and window material, may also be important when interpreting the data.[8] A considerable subset of target designs for HED experiments contains interfaces. Both particle and energy transport across these interfaces could affect material properties and dynamic processes.[9]

It is difficult to fully capture the kinetic processes in these high energy density systems because of the fast time scales of the corresponding ICF implosion or shock propagation, which are typically on the order of nanoseconds or shorter. In addition to these short time scales, the diffusion also occurs on a small spatial length scale near the material interface. Therefore, a deeper knowledge of these interface phenomena requires a diagnostic capable of detecting both these small spatial and temporal changes in the material.

An example of one such diagnostic is hard x-ray imaging using coherent sources, a technique that has applications in a wide variety of fields ranging from biology[10,11] to materials science.[12,13] While the state-of-the-art x-ray imaging of HED systems has achieved a spatial resolution of 3–10 μm,[14–17] advanced x-ray sources make it possible to image objects with sub-μm resolution[18,19] without a complicated setup, which is suitable for detecting interface dynamics for HED study. Furthermore, for multiple-material targets, tuning the incident x-ray energy to a value near the absorption edge of a specific material can enhance the contrast in the images. This way different ion species can be traced individually and therefore the mutual diffusion can be detected. Since these dynamic processes also strongly depend on temperature near the interface, simultaneous temperature diagnostics, such as emission spectroscopy,[20] are necessary to constrain the conditions. The fourth-generation x-ray free electron laser pulses are ideal for both coherent imaging and simultaneous fluorescence measurements.

Hard x-ray imaging together with the femtosecond time scales of x-ray free electron lasers enables the imaging of optically opaque materials that undergo rapid temporal and spatial changes, such as those that occur during shock propagation.[18] This has been demonstrated previously in diamond.[19] Here we show the capability of absorption–enhanced imaging above the Fe K-edge through comparison of simulated images with the experimental data of a two-material Fe_2O_3:SiO_2 aerogel system.

II. EXPERIMENTAL SETUP

The imaging experiments were carried out at the Matter in Extreme Conditions (MECs) endstation[21,22] of the Linac Coherent Light Source (LCLS), using a photon energy of

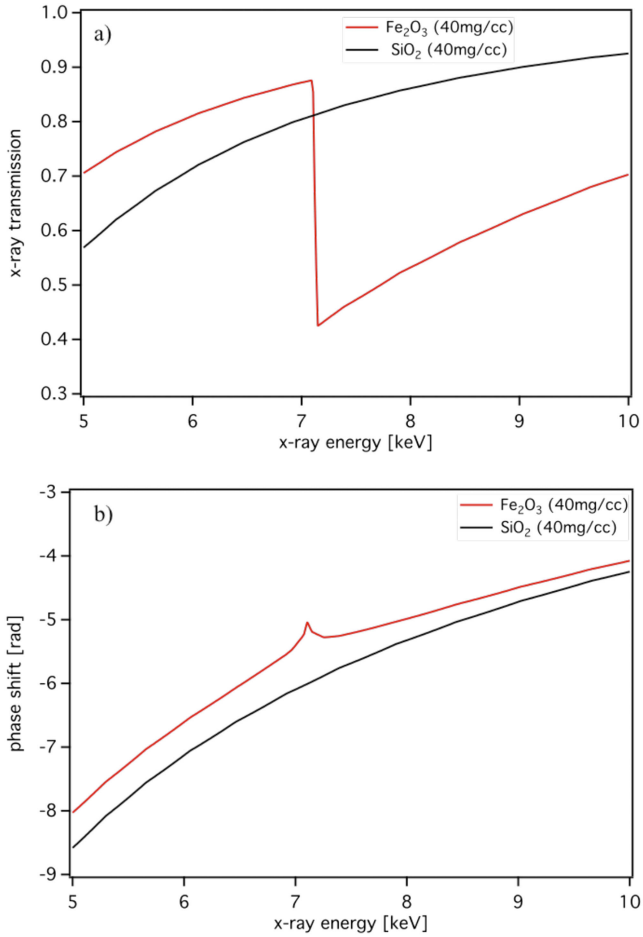

FIG. 1. (a) Transmission of x-rays through 1 mm-thick Fe_2O_3 (red) and SiO_2 (black) aerogel at 40 mg/cm^3. The contrast is enhanced near the Fe K-edge. (b) Phase shift of x-rays through 1 mm-thick Fe_2O_3 (red) and SiO_2 (black) aerogel at 40 mg/cm^3.

8.2 keV and an imaging setup similar to the one described previously in Ref. 19. The x-ray energy is above the Fe K-edge to enhance the absorption contrast of Fe ions relative to SiO_2 (Figure 1). A schematic of the setup is shown in Figure 2. For the experiments presented here, a set of 20 beryllium compound refractive x-ray lenses focused the incident LCLS x-ray beam to a spot size of 125 nm (full width half maximum), which served as the x-ray source at z_s = 222 mm in front of the sample for point projection. The images were recorded by a scintillator-based high-resolution x-ray detector positioned

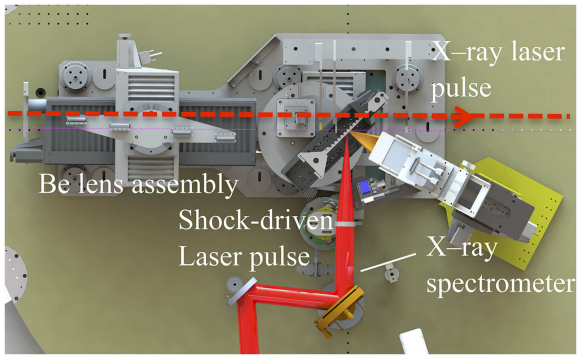

FIG. 2. Schematic of the experimental setup at the LCLS.

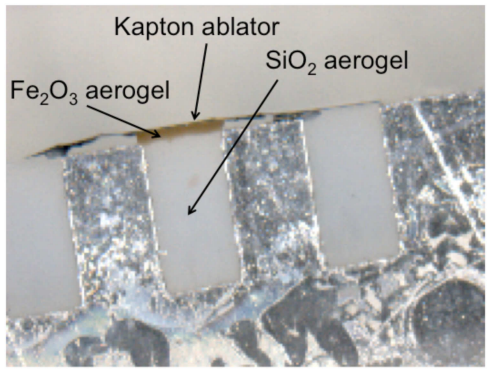

FIG. 3. Aerogel targets used in the imaging experiment.

at z_d = 4214 mm behind the sample. The magnification is thus M = $(z_s + z_d)/z_s$ = 20. The detector has a pixel size of p_d = 2.25 μm, corresponding to an effective pixel size of p = p_d/M = 112.5 nm in the object plane. The field of view in the target plane was approximately 250 μm in diameter.

The shock was generated by a 20 ns laser pulse irradiating the Kapton ablator at an intensity of ~1 × 10^{14} W/cm^2. Since the diffusion process is strongly dependent on temperature, Fe Kα x-ray fluorescence spectroscopy was also set up to infer the temperature in Fe_2O_3 after shock heating. The Kα line emission was induced by the same x-ray pulse and spectrally resolved using a von-Hamos crystal spectrometer provided by MEC.[23,24] The 30 × 32 mm^2 crystal, made of highly annealed pyrolytic graphite (HAPG), has a 2d spacing of 6.708 Å and

TABLE I. Values used for calculating the object wave field in the simulations.[29] The values at the experimental x-ray energy of 8.2 keV are also shown for comparison. All values are for a material density of 40 mg/cm^3.

X-ray energy (keV)	Material	δ	β
6.0	Fe_2O_3	$2.107\,067 \times 10^{-7}$	$4.288\,954 \times 10^{-9}$
	SiO_2	$2.342\,880 \times 10^{-7}$	$5.320\,324 \times 10^{-9}$
7.2	Fe_2O_3	$1.370\,949 \times 10^{-7}$	$1.545\,947 \times 10^{-8}$
	SiO_2	$1.621\,727 \times 10^{-7}$	$2.603\,796 \times 10^{-9}$
8.2	Fe_2O_3	$1.147\,706 \times 10^{-7}$	$9.798\,815 \times 10^{-9}$
	SiO_2	$1.247\,641 \times 10^{-7}$	$1.559\,917 \times 10^{-9}$

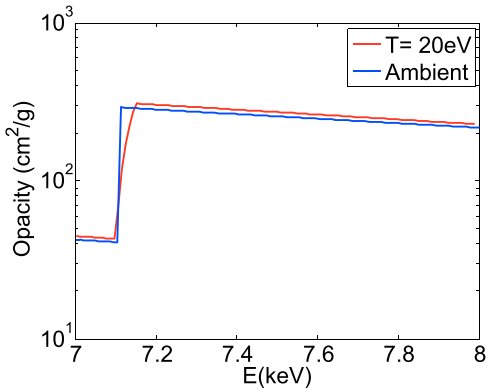

FIG. 4. Opacity of Fe at ambient temperature (blue) and at a temperature of 20 eV (red). The change in opacity with temperature is negligible beyond 7.2 keV.

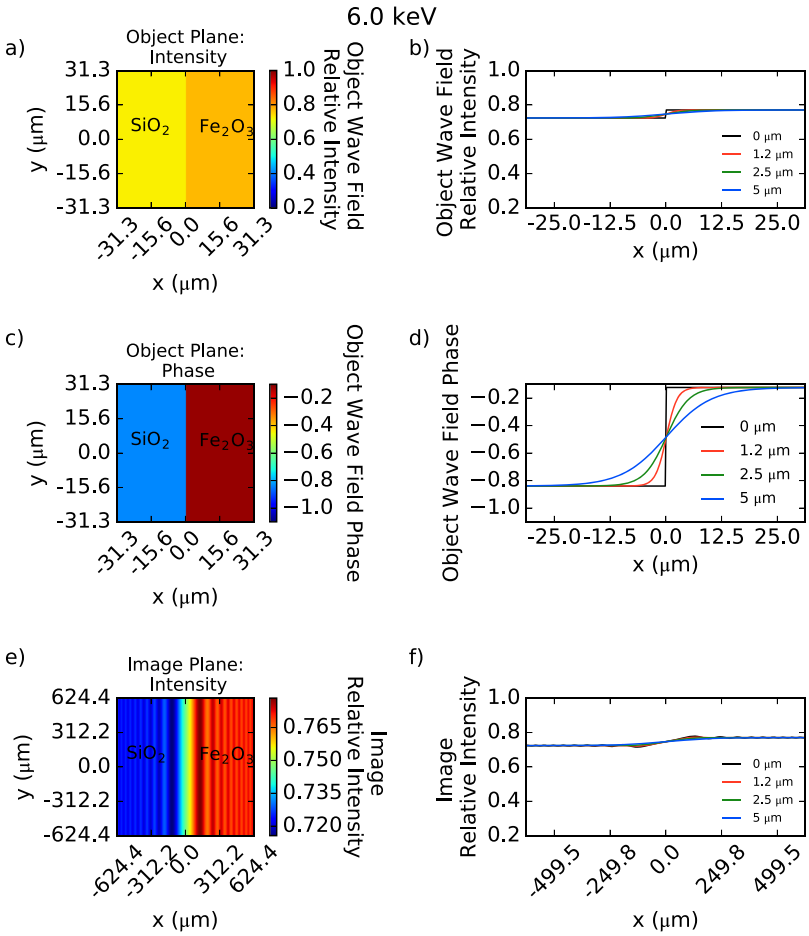

FIG. 5. Simulated images near the material interface of a Fe_2O_3:SiO_2 system (40 mg/cm^3, 1 mm thick) at an incident photon energy of 6.0 keV, which is below the Fe K-edge. (a) Intensity of the complex x-ray wave field behind the object. (b) Lineout of the intensity in (a) at y = 0 (black). Lineouts demonstrating the effects of particle diffusion at scales lengths of 1.2 μm (red), 2.5 μm (green), and 5.0 μm (blue) are also shown. (c) Phase of the complex wave field behind the object. (d) Lineout of the phase in (c) (black) and at three scale lengths. (e) Intensity of the wave field at the image plane. (f) Lineouts of the intensity in (e) (black) and at three scale lengths.

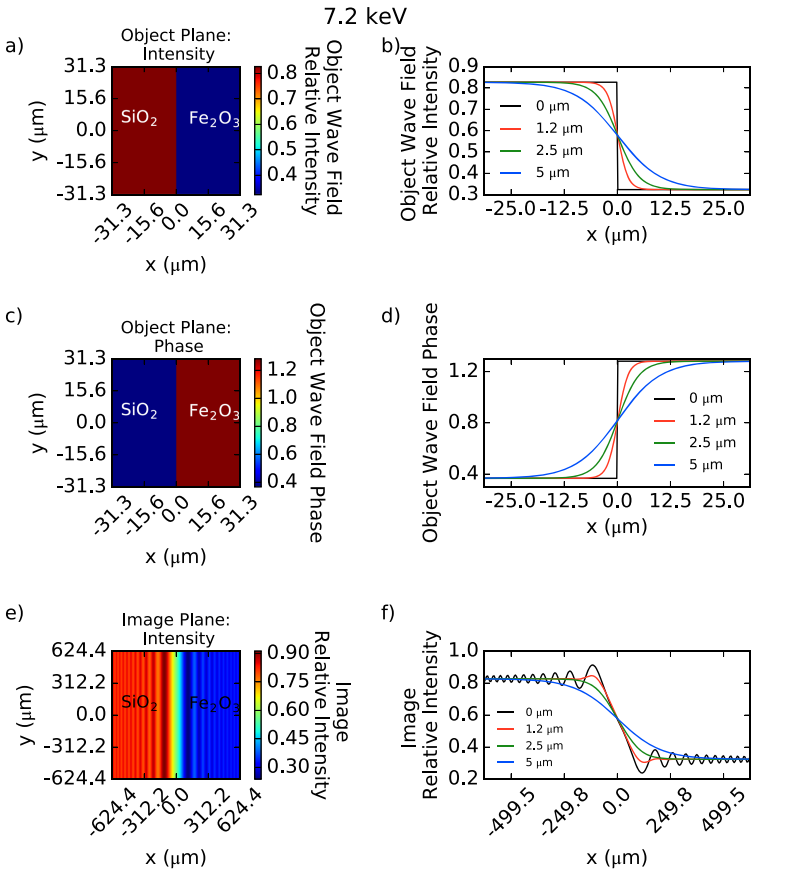

FIG. 6. Simulated images near the material interface of a Fe_2O_3:SiO_2 system (40 mg/cm^3, 1 mm thick) at an incident photon energy of 7.2 keV, which is just above the Fe K-edge. (a) Intensity of the complex x-ray wave field behind the object. (b) Lineout of the intensity in (a) at y = 0 (black). Lineouts demonstrating the effects of particle diffusion at scales lengths of 1.2 μm (red), 2.5 μm (green), and 5.0 μm (blue) are also shown. (c) Phase of the complex wave field behind the object. (d) Lineout of the phase in (c) (black) and at three scale lengths. (e) Intensity of the wave field at the image plane. The oscillations observed in the image are due to the sharp boundary separating the two materials. (f) Lineouts of the intensity in (e) (black) and at three scale lengths.

a radius of curvature of 51.7 mm. At focus, the 1:1 magnified spectrum is recorded with a Cornell-SLAC Pixel Array Detector (CSPAD), which is a direct detection X-ray camera with pixel size of 110 μm and an active area of 40×40 mm^2. The spectral resolution achieved was about 7 eV at 8.2 keV with a spectral range covering 7.8–8.6 keV. The good crystal reflectivity and collection angle allowed the K-alpha spectrum to be obtained in a single shot. The position, intensity, and width of the spectral peaks from Kα line emission are directly related to the state of the electrons. The ionization state of the atom can shift the energies of the Kα photons. When the temperature rises, the charge screening effect from the outer shell becomes weaker as more electrons are removed from the atom, resulting in a lowering of the energy levels due to the increase in binding energies. The inner shells shift more than the outer shells, and the difference between the energy levels increases as a result. This means that the Kα lines shift to higher energies with a higher degree of ionization at higher temperature.[25] In addition to this energy shift, ionization can also cause peak broadening.[26]

The initial timing between the optical laser and the x-rays was found using the signal of a fast photodiode looking at the fluorescence from a titanium foil (for the x-ray) or a YAG crystal (for the optical laser) at the interaction point. The rising edge of the long pulse laser is electronically overlapped with the rising edge of the x-rays using an SRS DG645 box. The convoluted signal of the x-ray signal can be overlapped with the optical laser rising edge within 100–200 ps. The RMS of the jitter between the arrival time of the optical laser vs the x-ray has been measured to be within ±50 ps. The delay between the pump and the probe was then controlled through the SRS box. The timing could be checked by looking at the difference between reference scope traces of diode signals of both arms on the oscilloscope in the laser enclosure and the signal coming from the delayed driven shots.

III. AEROGEL TARGETS

The Fe_2O_3:SiO_2 aerogel targets were fabricated using a procedure similar to the one outlined in Ref. 27. The targets had a density of 40 mg/cm^3 for each material. Along the shock direction, the target consisted of 50 μm Kapton as the ablator, 200 μm Fe_2O_3 aerogel, and 5 mm SiO_2 aerogel (Figure 3). The target was 1 mm thick both along the imaging axis and in the transverse direction. This dimension is large enough to delay any density release waves from the edges from entering the field of view. The original design was to study the Fe_2O_3 and TiO_2 interface as the x-ray energy can be tuned to both the Fe K-edge and the Ti K-edge. However, the TiO_2 aerogel encountered fabrication issues so the final targets were made of Fe_2O_3 and SiO_2. At 8.2 keV, the absorption is 55.7% in Fe_2O_3 and 12.2% in SiO_2, which is still good enough for absorption-enhanced imaging although only at the Fe side.

IV. SIMULATED IMAGES

In order to explore the capabilities of absorption-enhanced imaging, we have generated simulated images of a simple two-material system. The "sample" consists of separate portions of Fe_2O_3 and SiO_2, each with a density of 40 mg/cm^3 and a thickness of 1 mm in the x-ray propagation direction. Following the convention in Ref. 19, the two-dimensional exit wave field behind an object is given by the product of the incident x-ray probe function, P(x,y), and the object transmission function, O(x,y),

$$\psi_0(x,y) = P(x,y)\, e^{inkd(x,y)}, \tag{1}$$

$$= P(x,y)\, e^{-ik\delta d(x,y)} e^{-k\beta d(x,y)}, \tag{2}$$

$$= P(x,y)\; O(x,y), \tag{3}$$

where n is the complex-valued index of refraction, $k = 2\pi/\lambda$ is the wave vector of the incident x-ray radiation, and d(x,y) is the thickness of the material in pixel (x,y). In the hard x-ray regime, the refractive index is typically very close to 1 and is therefore written as $n = 1 - \delta + i\beta$, where δ defines the refractive index decrement, related to the phase shift introduced by the object, and β is the absorption index, related to x-ray absorption within the object. The values of δ_m and β_m (m = Fe_2O_3 or SiO_2) that were used in the presented simulations are given in Table I.

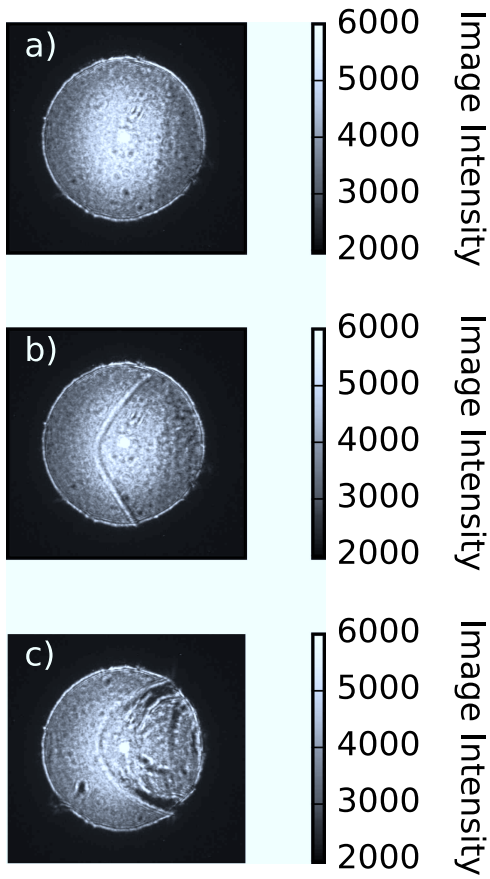

FIG. 7. (a) An image at 8.2 keV of the unshocked Fe_2O_3:SiO_2 target (40 mg/cm^3, 1 mm thick). The Fe_2O_3 is located to the right of the interface. There is a clear absorption enhanced contrast between the two materials. (b) An image at 8.2 keV of the shocked Fe_2O_3:SiO_2 target. The Fe_2O_3:SiO_2 boundary is less clearly resolved behind the shock front, indicating fracturing or diffusion between the two materials as a result of the shock. (c) An image of a shock inside the Fe_2O_3 aerogel, showing fractures behind the shock which could also contribute to the interface smearing in addition to diffusion. The material in the field of the view is all Fe_2O_3.

For the simulated images, the wave fields in the image plane were obtained by forward propagation of the object wave fields using the Fresnel propagator in the paraxial approximation,[28]

$$\Psi(X,Y) = \mathcal{F}_z[\psi_0(x,y)] = \frac{i}{z\lambda} e^{-2\pi i k z} \iint \psi_0(x,y) e^{\frac{-2\pi i[(x-X)^2+(y-Y)^2]}{2z}} dX dY, \quad (4)$$

where $\psi_0(x,y)$ is the object wave field, z is the propagation distance, and λ is the x-ray wavelength.

We note that the imaging simulations presented here were conducted using the refractive index values for Fe_2O_3 and SiO_2 at ambient temperature. Figure 4 shows the Fe opacity at ambient temperature and at a temperature of 20 eV (see Section V B).[30] The increased temperature will smear out the absorption spectrum near the K-edge energy in the vicinity comparable to the temperature (15–20 eV). The incident x-ray energy used in the imaging experiments, 8.2 keV, is well beyond the thermally broadened range in the absorption spectrum, and as such the use of the ambient temperature refractive index parameters in the simulations is valid.

Figures 5(a), 5(c), and 5(e) show the object wave field intensity, object wave field phase, and image intensity, respectively, after interaction of the "sample" with an x-ray probe at an incident photon energy of 6.0 keV (below the Fe K-edge). The corresponding lineouts at y = 0 are shown in Figures 5(b), 5(d), and 5(f), respectively. Figures 6(a)–6(f) show the object intensity, object phase, image intensity, and corresponding lineouts at y = 0 using an incident x-ray energy of 7.2 keV (slightly above the Fe K-edge). At 6.0 keV, the transmission through the SiO_2 side is slightly lower than the Fe_2O_3 side, whereas at 7.2 keV, the opposite trend is observed. This is expected due to the greater absorption of Si and Fe at 6.0 and 7.2 keV, respectively, resulting in lower intensities through those materials. There is also greater contrast between the SiO_2 and the Fe_2O_3 in the image plane at 7.2 keV compared to 6.0 keV (Figures 5(e), 5(f), 6(e), and 6(f)). Simulations using an incident energy of 8.2 keV, which was the x-ray energy used in the LCLS experiment, showed a trend similar to the one seen at 7.2 keV: higher absorption at the Fe_2O_3 side and lower absorption at the SiO_2 side. Therefore, the absorption profile can be directly related to Fe ions.

The object intensities in Figures 5(a) and 6(a), and object phases in Figures 5(c) and 6(c), represent an idealized case where there is a sharp flat boundary between the Fe_2O_3 and the SiO_2. This sharp boundary results in the oscillations seen in the final images. In reality, the material separation will likely be less well defined because of finite surface quality, and diffusion or mixing across the boundary. Figures 5(b) and 6(b) show lineouts of the wave field intensity in the case of particle diffusion near the material interface. Two Fermi-like functions were combined to model the simultaneous diffusion of the Fe_2O_3

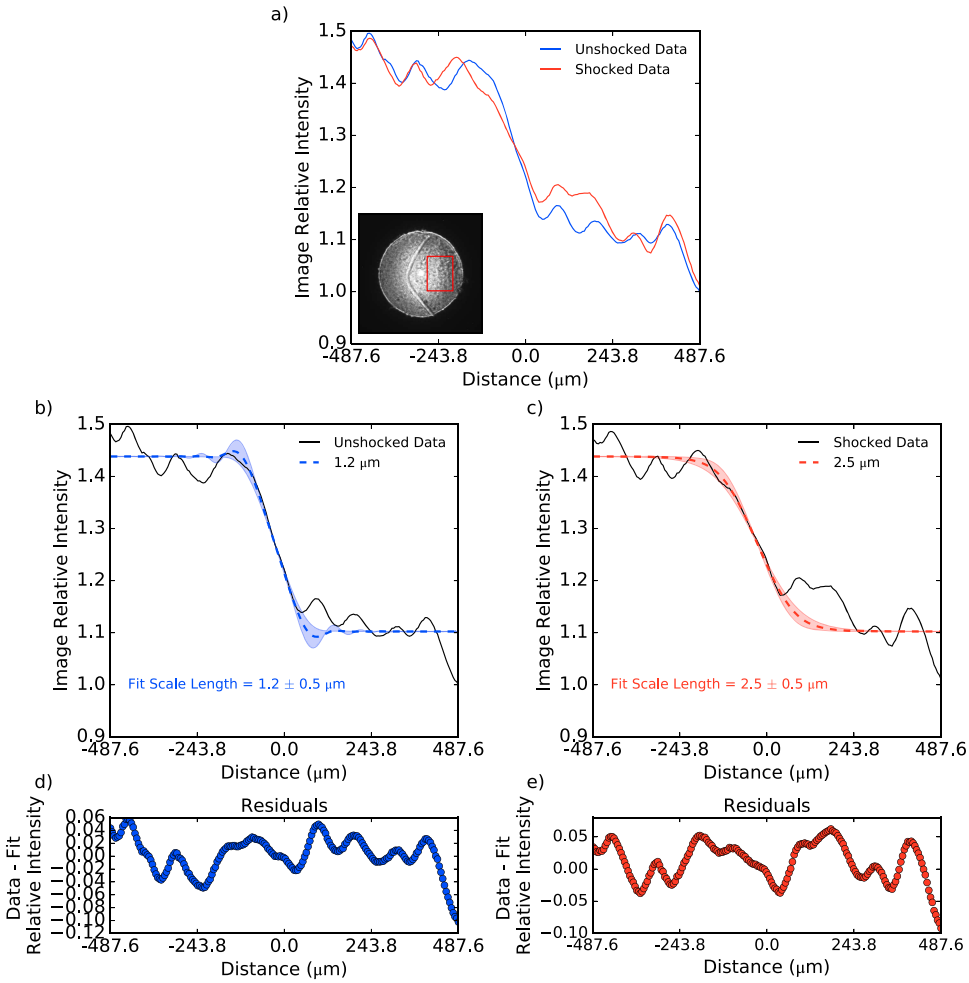

FIG. 8. (a) Lineouts of the averaged image data near the material interface before (blue) and after (red) the shock compression. The images were rotated by 8° to take the lineout along the interface. The inset shows the area in the images used for the average. (b) Lineout of the unshocked image near the material interface (black), and simulated image lineouts using an x-ray energy of 8.2 keV and Equation (5) with best-fit scale length and error bars. The simulated image lineouts have been renormalized to overlay the experimental data. (c) Same as (b) for the shocked image. The lineout of the shocked image has been renormalized to the maximum intensity of the unshocked image lineout. (d) and (e) show the residuals between the best-fit profile and the data.

and the SiO_2 across the interface,

$$y = \frac{\Psi_{SiO_2}}{e^{x/m} + 1} + \frac{\Psi_{Fe_2O_3}}{e^{-x/m} + 1}, \quad (5)$$

where ψ_{SiO_2} and $\psi_{Fe_2O_3}$ are the complex wave fields of the SiO_2 and Fe_2O_3, respectively, and m is the density scale length. The sign in the exponential indicates the diffusion direction.

Diffusion was modeled as three different scale lengths: 1.2 μm, 2.5 μm, and 5.0 μm. As the scale length of the diffusion increases, oscillations similar to those seen for the sharp boundary start to disappear at scale lengths of 1.2 μm and longer. This value is a useful threshold for the observed scale length of the diffusion when analyzing the experimental data.

V. EXPERIMENTAL DATA

A. X-ray images above Fe K-edge

Figures 7(a) and 7(b) show images at 8.2 keV of the Fe_2O_3:SiO_2 sample before and during the shock propagation. 8.2 keV is above the Fe K-edge where the absorption contrast is similar to that at 7.2 keV as shown in Figure 1(a). The shock reaches the interface at 5 ns. The image in Figure 7(b) was taken at 6 ns, i.e., 1 ns after the shock passes through the interface. In both images, the Fe_2O_3 has higher absorption compared to the SiO_2, as expected. The material interface is more distinct in the unshocked data, whereas after the shock, the boundary is smeared out. The image intensity changes after the shock are a reflection of both the fluctuations in the LCLS x-ray beam and the density changes that occur in the Fe_2O_3 and SiO_2 after shock compression. Both diffusion and other possible processes near the interface can result in the observed change in the sharpness of the interface. One of such processes is fracture development behind the shock, which can be clearly seen in another image taken for the shock inside the Fe aerogel shown in Fig. 7(c). Phase modulations can be seen at the shock front, indicating that such a setup is capable of resolving sub-micron scale lengths. The absence of phase modulations near the interface is due to finite interface smoothness.

Figure 8(a) shows lineouts near the interface before and after the shock compression. In order to more quantitatively assess the observed changes in the interface, simulated image lineouts were obtained via forward propagation of object wave fields calculated using the experimental x-ray energy of 8.2 keV and Equation (5) with different scale lengths, and then compared with the experimental data. Figures 8(b) and 8(c) show the unshocked/shocked data and the simulated image lineouts calculated using an object density of 40 mg/cm^3 and best-fit scale lengths with error bars. A scale length of 1.2 ± 0.5 μm gave the best match to the unshocked data, whereas a scale length of 2.5 ± 0.5 μm gave the best match to the shocked data. The residuals between the best-fit profiles and the data are displayed in Figs. 8(d) and 8(e), which are within 5%. The

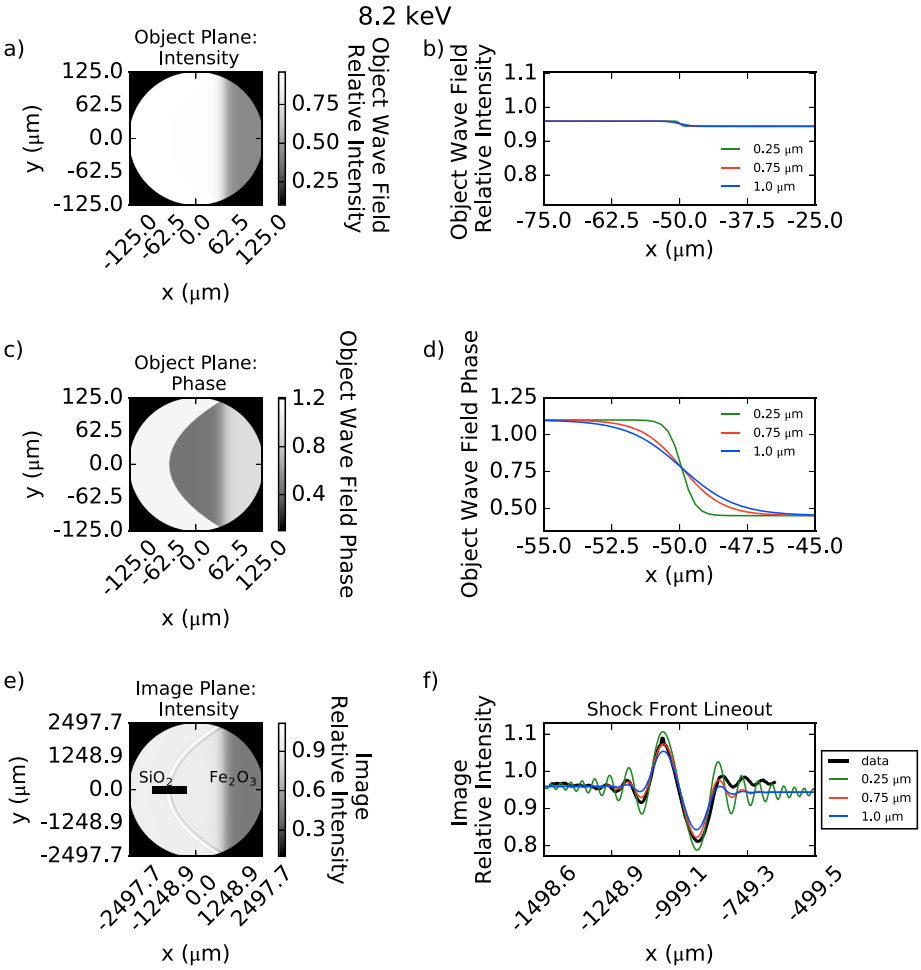

FIG. 9. (a) and (c) are the intensity and phase distributions in the objective plane. (b) and (d) are the corresponding lineouts near the tip of the shock front for three scale lengths, 0.25 μm, 0.75 μm, and 1.0 μm. (e) The simulated image with both shock front and the interface. The thick black line indicates where the lineout is taken. (f) Comparison between the data lineout near the shock front (black) and the simulated lineouts with three scale lengths.

longer scale length in the shocked sample supports the qualitative observation that the interface boundary is sharper in the unshocked data compared to the shocked data. It is noted that with the absence of phase modulations near the interface, a pure absorption analysis would give the same result. The increase in the scale length can be caused by a few mechanisms, such as diffusion and fractures developed near the interface as described above.

To further examine the actual resolution for the scale length in our experiment, we also analyzed the shock front data in Figure 7(b) using the same method as the interface. Figures 9(a) and 9(c) show the intensity and phase distributions in the objective plane, with the radius of curvature at the tip of the shock front matching the experimental data. The comparison of the simulated lineout at the shock front to the data is plotted in Figure 9(f) for three scale lengths, 0.25 μm, 0.75 μm, and 1.0 μm. It can be seen that the best fit of the shock front is 0.75 μm, while both 0.25 μm and 1.0 μm lineouts show clear deviation from the experimental data. This analysis confirms that our experimental setup is adequate for sub-micron resolution.

B. X-ray fluorescence spectroscopy

The raw images of the Fe Kα fluorescence spectra are shown in Figure 10. The change in the Fe Kα spectrum at different temperatures and densities was studied using the FLYCHK[31] code. FLYCHK solves rate equations for level population distributions by considering collisional and radiative atomic processes, and predicting K shell line emissions with various plasma conditions. Figure 11 shows calculated spectra as the temperature and density of the Fe change. The intensity of the $K\alpha_1$ peak is normalized to one. Figure 11(a) illustrates that when the temperature is below 20 eV, increasing the temperature mostly leads to a broadening effect in both the $K\alpha_1$ and $K\alpha_2$ peaks. At 20 eV, the two peaks merge into one peak with a shoulder. When the temperature is greater than 20 eV (Figure 11(b)), the line broadening effect is not obvious since the 2 peaks have already merged into one asymmetric peak, and a blue shift in the Kα position becomes dominant with increasing temperature.

When a shock passes through the Fe_2O_3 aerogel, it both heats and compresses the sample. Figure 11(c) shows the effect of sample density on the Kα spectrum. In this case, the temperature is kept the same (20 eV) and the density is increased from its original density of 40 mg/cm^3–400 mg/cm^3. The density increase mainly causes peak broadening, while the overall shape of the spectrum is not significantly changed. Therefore, density does not affect the spectrum as significantly as the temperature.

The experimental Fe Kα spectra are shown in Figure 12. The blue curve corresponds to the unshocked target while the red curve is measured 4 ns after the shock passes through the interface. The black solid line is the result from FLYCHK using the indicated temperature of 20 eV and a density of 40 mg/cm^3. Comparing the shocked and unshocked spectra, we find that the heating mainly causes a line broadening effect. The positions of the peaks stay almost the same. This observation indicates that the temperatures are all below 20 eV. By comparing the experimental spectra with spectra predicted by FLYCHK, we find that the sample is heated to roughly 15–20 eV. Figure 13 shows the temperature inferred from the Fe Kα spectra as a

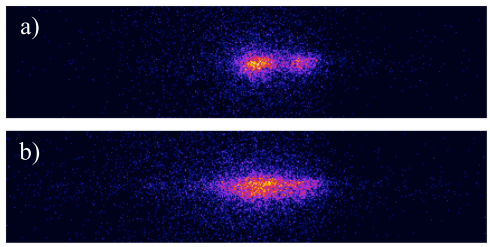

FIG. 10. (a) Raw Fe Kα image before the shot. Both the $K\alpha_1$ and the $K\alpha_2$ peaks are clearly seen. (b) Raw Fe Kα image during the shot. The $K\alpha_1$ and $K\alpha_2$ peaks are broader than before the shot.

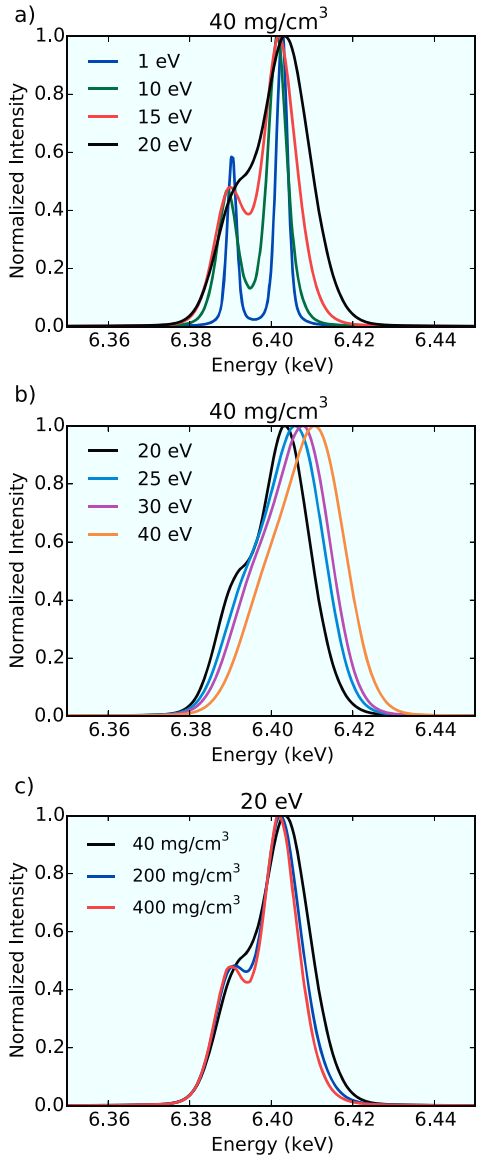

FIG. 11. Fe Kα spectra at different temperatures and densities calculated using FLYCHK. The intensity of the $K\alpha_1$ peak is normalized to one. (a) Kα spectra at different temperatures below 20 eV with a density of 40 mg/cm^3. (b) Spectra at different temperatures above 20 eV with a material density of 40 mg/cm^3. (c) Spectra at a temperature of 20 eV with different densities ranging from the original density (40 mg/cm^3) to 10 times the original density (400 mg/cm^3).

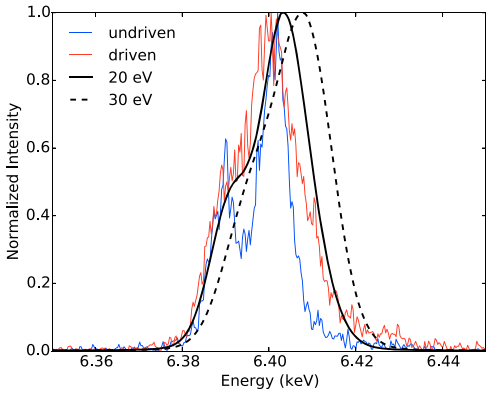

FIG. 12. Fe Kα spectra at an XFEL pulse delay of 9 ns. The intensity of the $K\alpha_1$ peak is normalized to one. The blue curve corresponds to the Fe Kα spectrum before the shock (undriven) while the red curve corresponds to the spectrum after the shock has passed through the interface (driven). The solid black curve is the FLYCHK spectrum at a density of 40 mg/cm^3 and at a temperature that produces a shape similar to the measured driven spectrum (20 eV). The dashed black line is the same density but with a higher temperature (30 eV). This illustrates that the peak shifts to higher energy if the temperature is higher.

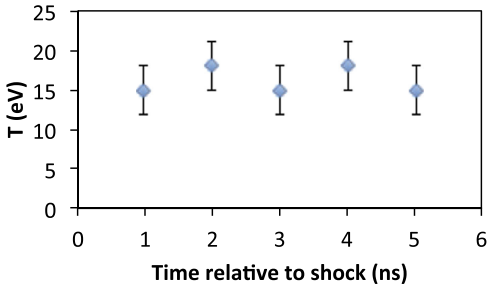

FIG. 13. Temperature inferred from Fe Kα spectra as a function of time relative to the shock front passage through the interface.

function of time relative to the shock front passage through the interface. No significant cooling was observed over time, which is consistent with the 20 ns duration of the driver pulse.

VI. DISCUSSION

Due to the limited interface quality of the target and possible fracture development in the aerogels after shock passage, the slightly longer scale length in the driven data cannot be solely attributed to diffusion. The scale length change from 1.2 μm (undriven) to 2.5 μm (driven) could provide an upper limit on the diffusivity across the interface. The data quality from this experiment was mainly affected by target quality. Hence the reproducibility also depends on the surface quality variation from target to target. For future experiments, the laser energy should be increased to achieve the desired temperature in the material (>50 eV) for more distinct diffusion features. In addition, the incident x-ray flatfield profile should be obtained on every shot to normalize the PCI images and cancel out the defects due to x-ray optics which affect the image quality. Improvements should also be made in the target fabrication for better-quality imaging data and to allow data acquisition for both sides of the sample.

VII. CONCLUSIONS

We have presented both simulated and experimental hard x-ray images of shocked Fe_2O_3 and SiO_2 aerogel foam materials using LCLS pulses. The simulations show dependence of the image on density profiles near the interface. Experimental data using an x-ray energy above the Fe K-edge demonstrate the enhanced contrast compared to below the Fe K-edge. Analysis of the experimental images shows that the density scale length near the Fe_2O_3:SiO_2 interface changes from 1.2 μm to 2.5 μm after the shock passes through, caused by both diffusion and other possible processes such as fractures near the interface. The temperature of shocked Fe_2O_3, measured using Kα x-ray fluorescence spectroscopy, is between 15 and 20 eV. The results highlight the potential for imaging at an x-ray absorption edge using LCLS pulses to detect ultrafast interface phenomena in dynamically compressed materials.

ACKNOWLEDGMENTS

Use of the Linac Coherent Light Source (LCLS), SLAC National Accelerator Laboratory, is supported by the U.S. Department of Energy, Office of Science, Office of Basic Energy Sciences under Contract No. DE-AC02-76SF00515. The MEC instrument is supported by the U.S. Department of Energy, Office of Science, Office of Fusion Energy Sciences under Contract No. SF00515. The authors thank A. Correa Barrios, S. Gammon, T. Baumann, and M. Biener for target fabrication. A. Schropp was supported by the Volkswagen Foundation and the DFG under Grant No. SCHR 1137/1-1. U. Zastrau was supported by the Volkswagen Foundation. The imaging setup at the LCLS was funded by the German Ministry of Education and Research (BMBF) under Grant No. 05K13OD2. B. I. Cho was supported by the NRF of Korea (Nos. NRF-2016R1A2B4009631 and NRF-2015R1A5A1009962). This work was performed under the auspices of U.S. DOE by Lawrence Livermore National Laboratory under Contract No. DE-AC52-07NA27344 with support from OFES Early Career program and LLNL LDRD program.

[1]H. G. Rinderknecht *et al.*, Phys. Rev. Lett. **114**, 025001 (2015).
[2]M. J. Rosenberg *et al.*, Phys. Rev. Lett. **112**, 185001 (2014).
[3]H. G. Rinderknecht *et al.*, Phys. Plasmas **21**, 056311 (2014).
[4]P. Amendt, C. Bellei, J. S. Ross, and J. Salmonson, Phys. Rev. E **91**, 023103 (2015).
[5]P. Amendt, S. C. Wilks, C. Bellei, C. K. Li, and R. D. Petrasso, Phys. Plasmas **18**, 056308 (2011).
[6]C. Bellei, P. A. Amendt, S. C. Wilks, M. G. Haines, D. T. Casey, C. K. Li, R. Petrasso, and D. R. Welch, Phys. Plasmas **20**, 044702 (2013).
[7]C. Bellei, H. Rinderknecht, A. Zylstra, M. Rosenberg, H. Sio, C. K. Li, R. Petrasso, S. C. Wilks, and P. A. Amendt, Phys. Plasmas **21**, 056310 (2014).
[8]E. Loomis, J. Hammerberg, J. C. Cooley, T. Shimada, R. P. Johnson, P. Peralta, R. Olson, and G. T. Gray, J. Appl. Phys. **117**, 185906 (2015).
[9]K. Molvig, E. L. Vold, E. S. Dodd, and S. C. Wilks, Phys. Rev. Lett. **113**, 145001 (2014).
[10]J. C. Andrews *et al.*, Microsc. Microanal. **16**, 327 (2010).
[11]E. Kosior, S. Bohic, H. Suhonen, R. Ortega, G. Deves, A. Carmona, F. Marchi, J. F. Guillet, and P. Cloetens, J. Struct. Biol. **177**, 239 (2012).
[12]S. Zabler, P. Cloetens, J. P. Guigay, J. Baruchel, and M. Schlenker, Rev. Sci. Instrum. **76**(7), 073705 (2005).

[13] A. W. Stevenson *et al.*, Nucl. Instrum. Methods Phys. Res., Sect. B **199**, 427 (2003).
[14] Y. Ping, O. L. Landen, D. G. Hicks, J. A. Koch, R. Wallace, C. Sorce, B. A. Hammel, and G. W. Collins, J. Instrum. **6**, P09004 (2011).
[15] C. Stoeckl *et al.*, Rev. Sci. Instrum. **85**, 11E501 (2014).
[16] B. Bachmann *et al.*, Rev. Sci. Instrum. **87**, 11E201 (2016).
[17] A. Do *et al.*, Rev. Sci. Instrum. **88**, 013701 (2017).
[18] A. Schropp, J. Patommel, F. Seiboth, B. Arnold, E. C. Galtier, H. J. Lee, B. Nagler, J. B. Hastings, and C. G. Schroer, in *X-Ray Free-Electron Lasers: Beam Diagnostics, Beamline Instrumentation, and Applications*, edited by S. P. Moeller, M. Yabashi, and S. P. HauRiege (SPIE-International Society Optical Engineering, Bellingham, 2012), Vol. 8504.
[19] A. Schropp *et al.*, Sci. Rep. **5**, 11089 (2015).
[20] S. B. Hansen *et al.*, Phys. Rev. E **72**, 036408 (2005).
[21] S. H. Glenzer *et al.*, J. Phys. B: At., Mol. Opt. Phys. **49**, 092001 (2016).
[22] B. Nagler *et al.*, J. Synchrotron Radiat. **22**, 520 (2015).
[23] U. Zastrau, A. Woldegeorgis, E. Forster, R. Loetzsch, H. Marschner, and I. Uschmann, J. Instrum. **8**, P10006 (2013).
[24] U. Zastrau *et al.*, Rev. Sci. Instrum. **85**, 109902 (2014).
[25] E. Martinolli, M. Koenig, J. M. Boudenne, E. Perelli, D. Batani, and T. A. Hall, Rev. Sci. Instrum. **75**, 2024 (2004).
[26] R. D. Cowen, *The Theory of Atomic Structure and Spectra* (University of California Press, 1981).
[27] S. O. Kucheyev, T. F. Baumann, C. A. Cox, Y. M. Wang, J. H. Satcher, A. V. Hamza, and J. E. Bradby, Appl. Phys. Lett. **89**, 041911 (2006).
[28] J. M. Cowley, *Diffraction Physics* (Elsevier Science, 1995).
[29] B. L. Henke, E. M. Gullikson, and J. C. Davis, At. Data Nucl. Data Tables **54**, 181 (1993).
[30] J. N. H. Magee, J. Abdallah, Jr., R. E. H. Clark *et al.*, in *Astrophysical Applications of Powerful New Databases*, edited by S. J. Adelman and W. L. Wiese (Astronomical Society of the Pacific, San Francisco, California, 1995), Vol. 78, p. 51.
[31] H. K. Chung, M. H. Chen, W. L. Morgan, Y. Ralchenko, and R. W. Lee, High Energy Density Phys. **1**, 3 (2005).